Three-dimensional dispersion in the type-II Dirac semimetals $PtTe_2$ and $PdTe_2$ revealed through circular dichroism in angle-resolved photoemission spectroscopy

Ivan Pelayo,[1,*] Derek Bergner,[1,*] Archibald J. Williams,[2] Jiayuwen Qi,[3] Penghao Zhu,[4] Mahfuzun Nabi,[1] Warren L. B. Huey,[2] Luca Moreschini,[5,6] Ziling Deng,[3] Tyler Hadsell,[1] Jonathan Denlinger,[7] Alessandra Lanzara,[5,6] Yuan-Ming Lu,[4] Wolfgang Windl,[3] Joshua Goldberger,[2] and Claudia Ojeda-Aristizabal[1,†]

[1]*Department of Physics and Astronomy, California State University Long Beach, Long Beach, California 90840, USA*
[2]*Department of Chemistry and Biochemistry, The Ohio State University, Columbus, Ohio 43210, USA*
[3]*Department of Materials Science and Engineering, The Ohio State University, Columbus, Ohio 43210, USA*
[4]*Department of Physics, The Ohio State University, Columbus, Ohio 43210, USA*
[5]*Department of Physics, University of California Berkeley, Berkeley, California 94720, USA*
[6]*Materials Sciences Division, Lawrence Berkeley National Laboratory, Berkeley, California 94720, USA*
[7]*Advanced Light Source, Lawrence Berkeley National Laboratory, Berkeley, California 94720, USA*

(Received 29 April 2024; revised 14 September 2024; accepted 31 October 2024; published 20 November 2024)

$PtTe_2$ and $PdTe_2$ are among the first transition metal dichalcogenides that were predicted to host type-II Dirac fermions, exotic particles prohibited in free space. These materials are layered and air stable, which makes them top candidates for technological applications that take advantage of their anisotropic magnetotransport properties. Here, we provide a detailed characterization of the electronic structure of $PtTe_2$ and $PdTe_2$ using angle-resolved photoemission spectroscopy (ARPES) and density functional theory calculations, offering an alternative interpretation for one of the Dirac-like dispersions in these materials. Through the use of circularly polarized light, we report a different behavior of such dispersion in $PdTe_2$ compared to $PtTe_2$, that we relate to a symmetry analysis of the dipole matrix element. Such analysis reveals a link between the observed circular dichroism and the different momentum-dependent terms in the dispersion of these two compounds, despite their close similarity in crystal structure. Additionally, our data show a clear difference in the circular dichroic signal for the type-II Dirac cones characteristic of these materials, compared to their topologically protected surface states. Our paper provides a useful reference for the ARPES characterization of other transition metal dichalcogenides with topological properties and illustrates the use of circular dichroism as a guide to identify the topological character and attributes of two otherwise equivalent band dispersions.

DOI: 10.1103/PhysRevB.110.195429

I. INTRODUCTION

$PtTe_2$ and $PdTe_2$ are known examples of topological semimetals created via a band inversion, with fourfold degenerate band touchings that are protected by time reversal T and inversion P symmetries. These band touchings are fourfold-degenerate Dirac points stabilized at the same crystal momenta by a C_3 symmetry along the rotation axis, and occur away from the time-reversal-invariant momentum (TRIM) [1]. In $PtTe_2$ and $PdTe_2$, these Dirac points host type-II excitations, that are only possible in a solid and have no counterpart in free space as they violate Lorentz invariance [2]; they were first predicted for certain Weyl semimetals, Dirac analogous where either T or P symmetries are broken [3,4], and were later predicted to appear in transition metal dichalcogenides such as $PtTe_2$ and $PdTe_2$ [5].

In general, materials with T and P symmetries and nonsymmorphic space groups (defined by the presence of either glide plane or screw axis symmetry) are characterized by Dirac nodes located at high symmetry points at the boundaries of the first Brillouin zone [6,7], also of importance in two dimensions [8,9]. In those materials, the presence of a Dirac cone depends on the nonsymmorphic character of the crystal space group, and it is known as an essential or symmetry-enforced band crossing. In contrast, in materials with symmorphic space groups such as $PtTe_2$ and $PdTe_2$, a Dirac cone results from a band inversion that is protected by the symmorphic crystal symmetries, such as C_3. They are less stable than the symmetry enforced Dirac cones, as they can disappear after tuning external parameters that do not compromise the crystal symmetry [1,6,10], and they are known as accidental band crossings [2]. In these materials, type-II fourfold degenerate Dirac points are formed by two twofold degenerate inverted bands that have different rotation eigenvalues. This was also the case in the first predicted [11,12] and later experimentally realized type-I Dirac semimetals, Na_3Bi [13] and Cd_3As_2 [14–16]. As a result of T and P symmetries, the type-II Dirac dispersions in $PtTe_2$ and $PdTe_2$ come in pairs at points in momentum space along the rotation axis, away from high symmetry points such as Γ or A.

The experimental signature of Lorenz-violating type-II Dirac excitations in $PtTe_2$ and $PdTe_2$ was first obtained through angle-resolved photoemission spectroscopy (ARPES)

*These authors contributed equally to this work.
†Contact author: claudia.ojeda-aristizabal@csulb.edu

experiments [17,18], supported by first principles calculations. Interestingly, these and previous experiments [19] found evidence that these materials have, in addition to the type-II Dirac dispersions, topologically nontrivial surface states. Such states derive from band inversions and connect gapped bulk bands.

Although both three-dimensional (3D) Dirac dispersions and surface state cones arise from band inversion, their properties are fundamentally different. For instance, the three-dimensional type-II Dirac cone is associated to gapless matter, and it is formed by a four-band crossing leading to the previously mentioned fourfold degenerate Dirac point preserved by the crystal's C_3 rotational symmetry. It is not topologically protected as the associated topological invariant, the total Chern number of the bands, is zero [20]. Indeed, the type-II Dirac cone results from the merging of Weyl points at opposite momenta with opposite Chern numbers. In contrast, the Dirac surface states are typically associated to three-dimensional bulk insulators with important spin-orbit coupling and time-reversal symmetry. Such surface states are metallic, chiral (the spin of the electrons is linked to their direction of motion), and, most importantly, topologically protected.

The different nature of these linear dispersions in Dirac semimetals manifests experimentally in different ways. In ARPES, the topological protected surface states present a switching of the circular dichroic signal across the Dirac point, related to their chiral character. In contrast, the three-dimensional type-II cones present no switching, as they are formed by twofold degenerate bands. Here we present an analysis of the band structure of $PtTe_2$ and $PdTe_2$ through ARPES and density functional theory (DFT) calculations that show proof of an additional dispersion that presents no switching in the circular dichroism (CD) for $PtTe_2$ and a clear switching for $PdTe_2$. We understand our observation through a symmetry analysis of the dipole matrix elements that relate to the observed ARPES intensity, showing that even though these materials belong to the same space group, they present a dispersion that is dominated by a linear term in momentum in the case of $PtTe_2$ and a cubic term in the case of $PdTe_2$. Additionally, our photoemission data using circularly polarized light present further evidence of the different character of the known type-II Dirac cones and topologically protected surface states in $PtTe_2$ and $PdTe_2$.

II. METHODS

Single crystals of $PtTe_2$ were grown from a flux of Pt powder and Te chunks (see Supplemental Material [21], which includes Refs. [22,23], for details). The grown crystals presented lattice constants of $a = b = 4.025$ Å and $c = 5.224$ Å [24]. Single crystals of $PdTe_2$ were grown from a stoichiometric melt of Pd powder and Te lump. X-ray diffraction (XRD) experiments demonstrated that $PdTe_2$ crystallizes into a one-layer trigonal unit cell with a $P\bar{3}m1$ space group. The measured lattice constants were $a = b = 4.037$ Å and $c = 5.130$ Å [24]. High resolution ARPES experiments were performed at Beamline 4.0.3 (MERLIN) of the Advanced Light Source at the Lawrence Berkeley National Laboratory in a vacuum better than 5×10^{-11} Torr using 30–128-eV linearly and circularly polarized photons. The total energy resolution was 20 meV with an angular resolution $\Delta\theta \leqslant 0.2^\circ$. Measurements were taken at 10 K. The density functional theory calculations were performed on $PtTe_2$ and $PdTe_2$ primitive cells using the Vienna Ab Initio Simulation Package [25,26] with Perdew-Burke-Ernzerhof functionals [27,28]. The relaxed electronic configurations were obtained using a $4 \times 4 \times 3$ k-point grid and a plane-wave energy cutoff of 250 eV for $PtTe_2$ and 270 eV for $PdTe_2$. The convergence of the electronic structure with respect to the chosen cutoff energies is shown in Fig. S1 of Supplemental Material [21]. The lattice parameters were fixed to $a = b = 4.0259$ Å and $c = 5.2209$ Å for $PtTe_2$ [29]; $a = b = 4.0420$ Å and $c = 5.1253$ Å for $PdTe_2$ [30]. Spin-orbit coupling was included in both cases.

III. ARPES MEASUREMENTS AND DFT CALCULATIONS

Figures 1(e)–1(g) show the crystal structure and first Brillouin zone of the two compounds studied in this paper, $PtTe_2$ and $PdTe_2$. These compounds, similarly to $PtSe_2$ and $PtBi_2$, crystallize into space group $P\bar{3}m1$ (no. 164). They are layered, with Te atoms that sandwich the Pt (or Pd) atoms and with the Te atoms within each layer related by inversion symmetry [5]. Space group $P\bar{3}m1$ has a primitive Bravais lattice with inversion symmetric threefold rotation and mirror symmetry. In such a unit cell (see Fig. S2 of Supplemental Material [21]), there are three mirror planes that coincide with the M-Γ-A planes in momentum space, highlighted in blue in Fig. 1(e). From these symmetries derive the main features of interest in $PtTe_2$ and $PdTe_2$, indicated by arrows in Figs. 1(a) and 1(b), namely, (1) a type-II Dirac cone at -1 and -0.6 eV for $PtTe_2$ and $PdTe_2$ respectively (red arrows), (2) conical dispersions at -2.25 eV for $PtTe_2$ and at -1.7 eV for $PdTe_2$ that correspond to surface state Dirac cones (black arrows), and (3) a Dirac-like dispersion at -1.4 eV for $PtTe_2$ and -1.1 eV for $PdTe_2$ (blue arrows) for which we give an interpretation that is different from the one existing in the literature [31,32]. The data presented in Fig. 1 were taken at photon energies close to the type-II Dirac cone D, located at $k_z{=}\Gamma \pm 0.37c^*$ for $PtTe_2$ and $k_z{=}\Gamma \pm 0.40c^*$ for $PdTe_2$. For $PtTe_2$ we used $h\nu{=}68$ eV, close to $k_z = 3.63c^*$, as well as $h\nu = 98$ eV, close to $k_z = 4.37c^*$. We considered an inner potential of $V_0{=}12$ eV, with $c^*{=}2\pi/c$ and $c = 5.224$ Å, deduced from XRD experiments. In the case of $PdTe_2$, data were collected using $h\nu = 60$ eV, close to $k_z = 3.60c^*$ assuming an inner potential of $V_0{=}16$ eV with $c = 5.130$ Å (see Tables I and II in Supplemental Material [21]). In both cases, we used p-polarized photons. The inner potential value was chosen after matching symmetric scans along the M-Γ-M direction to the high symmetry points Γ and A, since all the other cuts do not have mirror symmetry in this crystallographic direction.

Figures 1(c) and 1(d) show constant energy maps at the Fermi level for $PtTe_2$ and $PdTe_2$ respectively, where we can observe a threefold symmetry. Overall, we notice a broadening of the bands for $PtTe_2$ compared to $PdTe_2$. This can be related to the way these crystals are grown (see Supplemental Material [21]). $PtTe_2$ is grown from a Te flux that requires a quenching and centrifuging off the Te flux at $\approx$500 °C. In contrast, $PdTe_2$ is obtained from a melt grown that is let to cool down to room temperature naturally, leading likely to higher quality crystals.

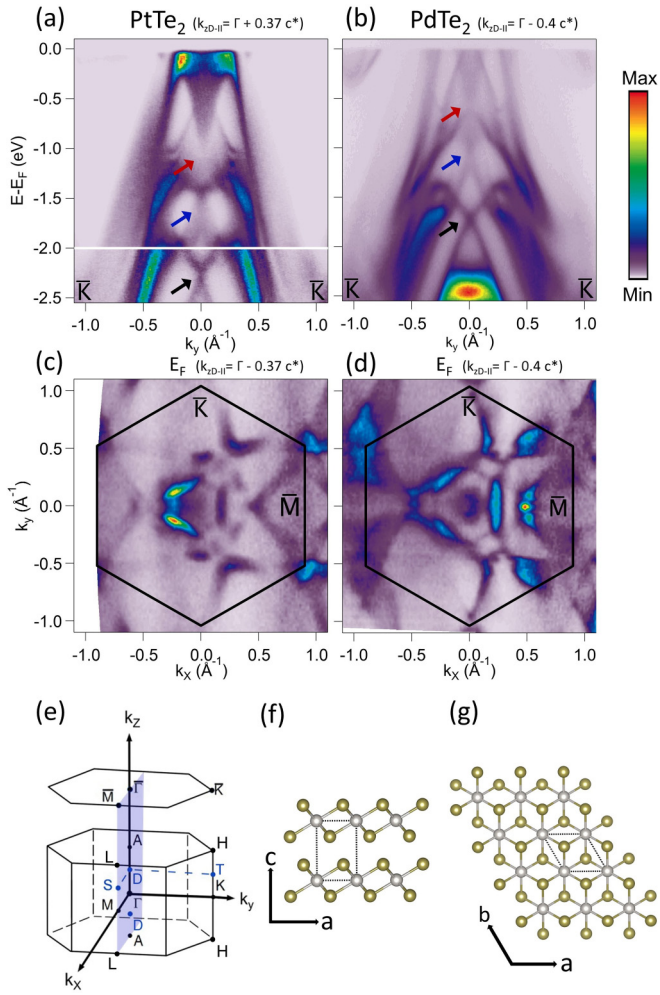

FIG. 1. $PtTe_2$ and $PdTe_2$ high resolution ARPES band structure and Fermi surface using linearly p-polarized photons. (a) Data for $PtTe_2$ at $h\nu = 98$ eV, the top type-II Dirac point D ($k_z = 4.37c^*$) along the $\overline{K}$-$\overline{\Gamma}$-$\overline{K}$ direction showing the type-II cone (red arrow), surface state cone (black arrow), and 3D Dirac-like dispersion (blue arrow). (b) Data for $PdTe_2$ at $h\nu = 60$ eV, very close to the bottom type-II Dirac cone D ($k_z = 3.55c^*$) along the $\overline{K}$-$\overline{\Gamma}$-$\overline{K}$ direction. Arrows show the same Dirac dispersions as in (a). Fermi surface for (c) $PtTe_2$ and (d) $PdTe_2$ at $h\nu = 68$ eV, close to the bottom type-II Dirac point D ($k_z = 3.63c^*$) and $h\nu = 60$ eV ($k_z = 3.55c^*$, close to the bottom D $k_z = 3.60c^*$) respectively. (e) First Brillouin zone for both compounds showing the pair of type-II Dirac points and one of the three mirror planes along M-Γ-A. (f) Crystal structure for both compounds showing the transition metal atoms (white) sandwiched in between the Te atoms (gold). (g) In-plane crystal structure for both compounds.

The observed three-dimensional surface states in both compounds have been identified in the past as topologically nontrivial [5,17,19]. Indeed, both the $PtTe_2$ and $PdTe_2$ surface states have been associated to a band inversion at TRIM A [5,17], and calculations of the time-reversal invariant Z_2 for these states have confirmed their nontrivial character [5,17,19]. Our DFT calculations presented in Fig. 2 are sensitive to the orbital character of the bands. They show that at TRIM A, where the band inversion that leads to the

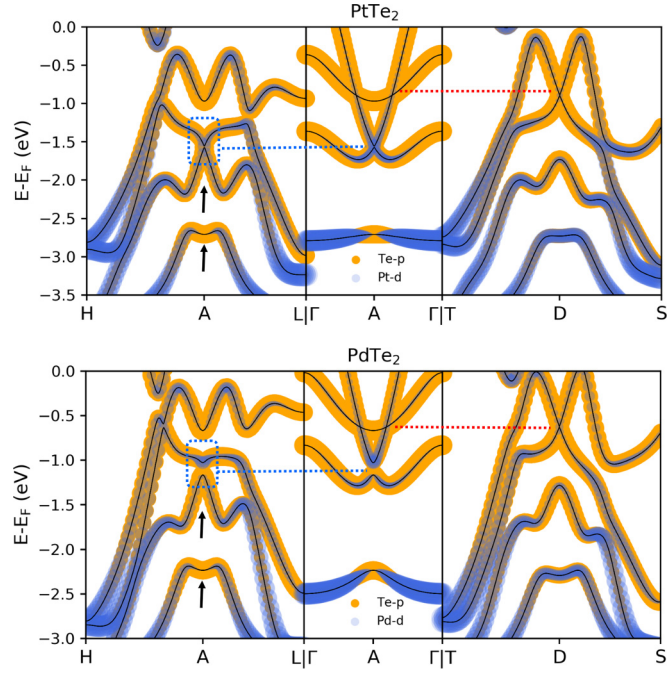

FIG. 2. $PtTe_2$ and $PdTe_2$ DFT calculations showing the type-II cone along Γ-A-Γ and T-D-S (red pointed line), the bulk bands that lead to the topologically protected surface state cone (black arrows) and the three-dimensional dispersions (blue pointed lines). The calculations show the contribution of Te-p and Pd-d orbitals to the different bands.

topologically protected surface state occurs, they are mainly of Te-p character. We also identify in our calculations the 3D type-II cones for both compounds, indicated by horizontal red pointed lines along Γ-A-Γ and T-D-S. We find that bands that host the type-II excitations are also of Te-p type, as previously reported [17]. Most importantly, we see evidence of the additional dispersion spotted in our ARPES data, discernible along the high symmetry directions H-A-L and Γ-A-Γ in both $PtTe_2$ and $PdTe_2$ (indicated by pointed blue lines). Although this dispersion appears to be Dirac-like and has been identified in the past as a topologically protected surface state in $PdTe_2$ [31,32], we believe that it has a bulk character, given the energy range which this dispersion spans. Specifically, the bulk bands that previous works have labeled as responsible for the topologically protected surface state [32] form a gap that is very small to host the experimentally observed Dirac-like dispersion. Even if there are topologically protected surface states, they are only sharply localized at the edge within the narrow bulk gap. Outside of this small energy interval corresponding to the bulk gap, the surface states will strongly hybridize with the bulk states. Therefore, phenomena such as the observed dichroism over a much larger energy window, as will be developed later, should be understood primarily through a theory of bulk states. If one considers that the Dirac-like dispersions at -1.1 eV for $PdTe_2$ and -1.4 eV for $PtTe_2$ are bulk states, the point group symmetry at momentum A does not allow a fourfold degenerate Dirac point at A. The four bands that are related to the observed dispersion form a representation where both the threefold rotation operator and the inversion operator are diagonal [23]. It is expected

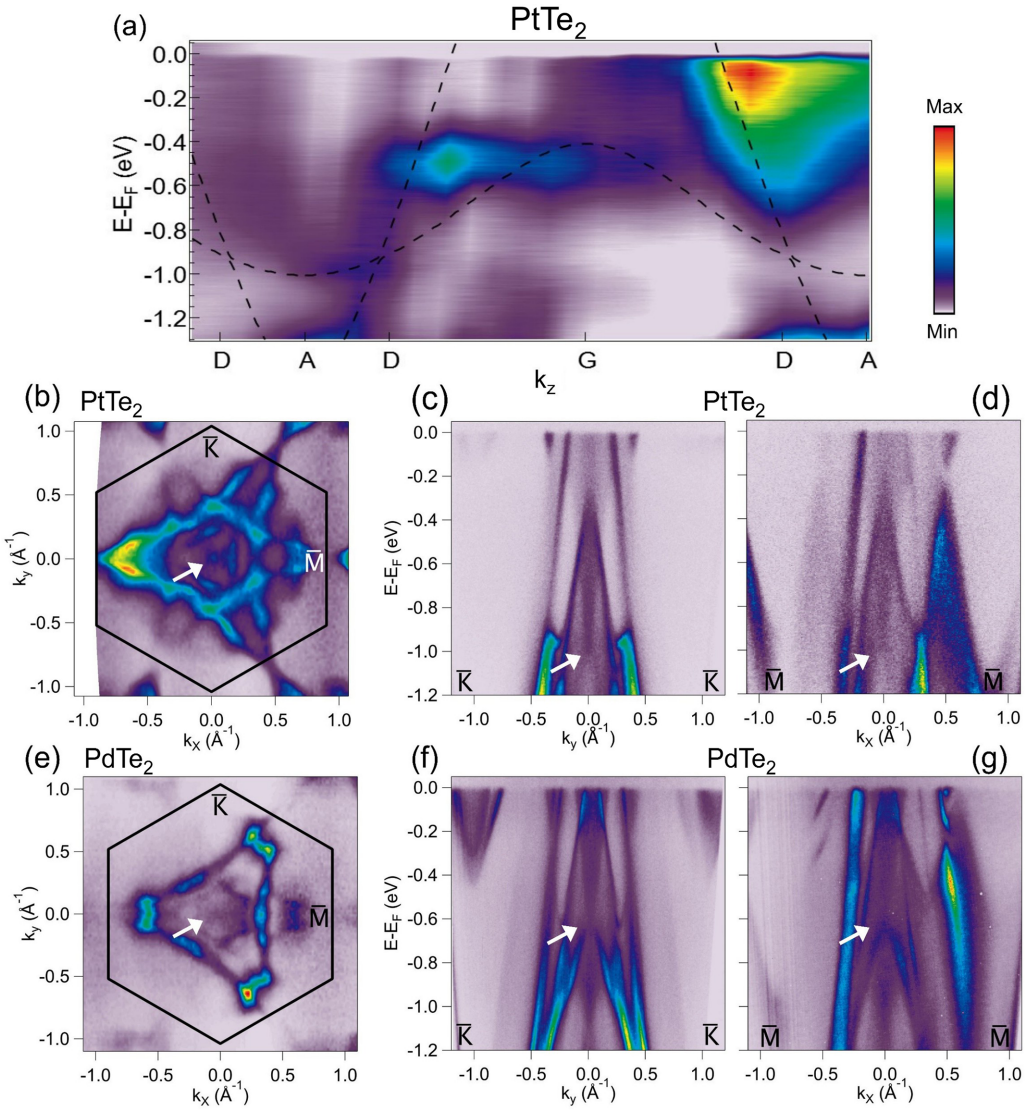

FIG. 3. ARPES band structure of $PtTe_2$ and $PdTe_2$ obtained using linearly p-polarized light. (a) Measured $PtTe_2$ dispersion using $h\nu$ range $\approx$ 50–105 eV along the k_z direction at $k_x = k_y$=0 superimposed with DFT bulk calculations showing the type-II Dirac cone band crossing at D. (b) Data for $PtTe_2$ at $h\nu$=68 eV ($\Delta k_z \approx 0.05c^*$ from D) showing a constant energy map at $E - E_F \approx -1$ eV, corresponding to the type-II Dirac point (white arrows). (c), (d) Dispersions along the (c) $\overline{K}$-$\overline{\Gamma}$-$\overline{K}$ and (d) $\overline{M}$-$\overline{\Gamma}$-$\overline{M}$ directions. (e)–(g) Equivalent data for $PdTe_2$ using $h\nu$ = 60 eV ($\Delta k_z \approx 0.05c^*$ from D) (e) at $E - E_F \approx -0.6$ eV and along the (f) $\overline{K}$-$\overline{\Gamma}$-$\overline{K}$ and (g) $\overline{M}$-$\overline{\Gamma}$-$\overline{M}$ directions.

therefore that along the Γ-A direction the energy dispersion is even in k_z and therefore nonlinear. As a consequence, this dispersion is gapped in both materials, presenting a larger gap for $PdTe_2$. Indeed, our DFT calculations predict this gap to be 16 meV for $PtTe_2$ and 138 meV for $PdTe_2$, however these values appear to overestimate the actual gap size, which prevents us from confirming it experimentally. Interestingly, this dispersion shows a different dichroic signal for the two materials, as will be developed later.

We start by discussing in detail the experimental signature of the linear dispersion that hosts exotic type-II fermions, shown in Fig. 3. Evidence of such excitations has been reported in the literature as strongly tilted Dirac cones resulting from the merging of topologically protected touching points between electron and hole pockets [5,17]. Similar to their type-I counterparts, type-II Dirac particles are described by a massless Dirac Hamiltonian. However, in the case of type-II particles, the dispersion relation is not the same in all three directions of momentum, which breaks particle-hole symmetry and the Lorentz invariance. This is prohibited in quantum field theory, as free space is isotropic, but it is permitted in a solid. The key features of such a type-II cone can be understood by adding a tilt to the Dirac Hamiltonian in the Weyl representation:

$$H_{\pm} = \pm v_F \boldsymbol{\sigma} \cdot \mathbf{k} + \mathbf{t} \cdot \mathbf{k} I_2$$

where v_F is the Fermi velocity, $\boldsymbol{\sigma}$ are the 2×2 Pauli matrices, I_2 is the identity matrix, and $\mathbf{t}$ is the tilt vector [2,4]. In $PtTe_2$ and $PdTe_2$ the tilt is along the k_z direction, where $tk_z > v_F k_z$. Therefore in a type-II Dirac semimetal, instead of a pointlike Fermi surface at the $k_\parallel$-k_z plane, there are open electron and hole pockets that touch at points. Demonstration of type-II excitations for $PdTe_2$ requires a careful comparison of the measured dispersions at different k_z with first principle

calculations [18], as is shown in Fig. S3 of Supplemental Material [21]. In the case of $PtTe_2$, a clear signature of a tilted cone can be measured along the out-of-plane momentum k_z, as shown in Fig. 3(a), consistent with our first principles calculations. Final state effects make the type-II cone visible only at $h\nu = 65$ eV, corresponding to $k_z = 3.63c^*$. The existence of not only one but two type-II Dirac points within the same Brillouin zone (along the rotation axis of the crystal) is a consequence of the time reversal T and inversion P symmetries of these materials. Our DFT calculations predict this to happen at $k_z{=}\Gamma \pm 0.37c^*$ for $PtTe_2$ and $k_z{=}\Gamma \pm 0.40c^*$ for $PdTe_2$, that corresponds in our experiment to $h\nu = 65$ and 98 eV for $PtTe_2$ and $h\nu = 62$ and 99 eV for $PdTe_2$, with $\Gamma = 4c^*$ for both compounds (check Tables I and II in Supplemental Material [21]). The type-II Dirac cones are visible along the $k_\parallel$ directions, where they appear as straight cones, seen in Figs. 3(c) and 3(d) for $PtTe_2$ and Figs. 3(f) and 3(g) for $PdTe_2$. The type-II Dirac points can also be seen in the constant energy maps shown in Figs. 3(b) and 3(e), as small dots at the center of the first Brillouin zone can be discerned. Data for the pairs of type-II Dirac cones in each material are shown in Fig. S5 of Supplemental Material.

The use of circularly polarized light can serve as a guide to identify the three-dimensional Dirac dispersions from the topologically protected surface states. Despite the fact that the difference in photoemission using left- vs right- circularly polarized light, known as circular dichroism, is known to be strongly dependent on final states and not a reliable tool to probe the spin polarization of the initial states [33–35], CD can provide information on the initial states' relative alignment across different binding energies in the band structure [34]. For instance, soon after the discovery of the first 3D topological insulators, CD was used to help map the spin-orbit texture of the surface states in those materials [36,37]. Indeed, in the presence of spin-orbit coupling, the electron states are best described by their total angular momentum instead of their spin, and since the helicity of light in ARPES experiments couples to the electron's total angular momentum, it indirectly pairs to the spin of the material electrons [38]. As a result, one can measure ARPES that is helicity dependent for linear topological surface states.

Figure 4 (top) shows the geometry of the experimental setup. Circularly polarized light is incident in the $k_y{=}0$ plane, 65° with respect to the analyzer lens, which breaks any geometrical symmetry with respect to the $k_x{=}0$ plane (yellow plane in Fig. 4). As a consequence, there is no symmetry in the photoemission measured between $\pm k_x$ points for different light polarizations. In contrast, there is a generic geometrical dichroism above and below the $k_y{=}0$ incident plane (at $\pm k_y$ for any k_x) provided that the crystal has also a symmetry with respect to the $k_y{=}0$ plane. We present in Figs. 4(a)–4(f) the measured CD for $PtTe_2$ and $PdTe_2$ along the $\overline{K}$-$\overline{\Gamma}$-$\overline{K}$ and $\overline{M}$-$\overline{\Gamma}$-$\overline{M}$ directions in different binding energy ranges. We used photon energies very close to the type-II Dirac cone. To obtain a geometrical dichroism at each measurement, the azimuth angle of the sample was adjusted to have $\overline{K}$-$\overline{\Gamma}$-$\overline{K}$ or $\overline{M}$-$\overline{\Gamma}$-$\overline{M}$ along the direction of the detector [yellow plane in Fig. 4(a)]. As previously mentioned, the existence of a dichroic signal relies not only on the geometry of the experimental setup but also on the symmetry of the crystal across the incident plane (blue plane in Fig. 4). Because in $PtTe_2$ and $PdTe_2$ there is a mirror plane along M-Γ-A, a symmetric photoemission is observed when such mirror plane is aligned to the blue plane in Fig. 4, that is, along $\overline{K}$-$\overline{\Gamma}$-$\overline{K}$ rather than $\overline{M}$-$\overline{\Gamma}$-$\overline{M}$. This can

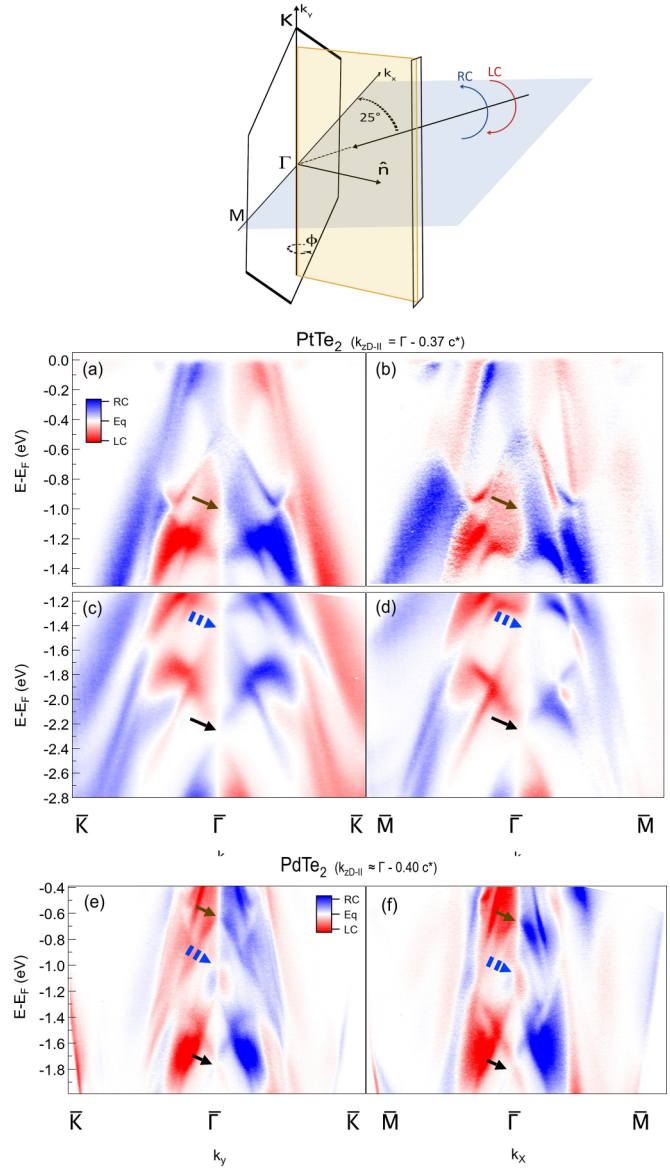

FIG. 4. Circular dichroism for $PtTe_2$ and $PdTe_2$. Top: Schematics of the experimental setup at the ALS Beamline 4. Incident photons are right-hand (blue) or left-hand (red) circularly polarized. Photons are incident on the blue plane 25° with respect to the surface of the sample, or 65° with respect to the normal of the sample $\hat{n}$. The detector plane is indicated in orange. Φ is the polar angle that allows us to tune the angle of the sample into normal emission ($\Phi = 0$). Middle: Circular polarization dependent photoemission for (a)–(d) $PtTe_2$ and (e), (f) $PdTe_2$ along $\bar{K}$-$\bar{\Gamma}$-$\bar{K}$ and $\bar{M}$-$\bar{\Gamma}$-$\bar{M}$, displaying the type-II Dirac cone (top brown arrows), the Dirac-like crossing that we ascribe to a bulk dispersion (middle blue arrows), and Dirac surface states (bottom black arrows). Data for $PtTe_2$ were taken at 66-eV photon energy, near $k_z = 3.63c^*$, the type-II cone D. Data for $PdTe_2$ were taken at 60 eV, close to $k_z = 3.60c^*$, the D point ($\Delta k_z \approx 0.05c*$ from D).

be seen when comparing scans along these two high symmetry directions in Figs. 3 and 4.

In general, CD is absent when a symmetry operation that transforms right into left circularly polarized light leaves the momentum of the photoelectrons **k** unaffected. This happens at the plane k_y=0 [blue plane in Fig. 4(a)], where a mirror transformation changes right into left circularly polarized light without affecting **k**, that is parallel to the normal $\hat{n}$ of the sample. There should be therefore zero CD for k_y=0. In contrast, along the k_x=0 plane (yellow plane), a reversal of the light polarization changes the sign of the y component of **k**, resulting in a nonzero CD. This can be observed when comparing the circular dichroism data along $\overline{K}$-$\overline{\Gamma}$-$\overline{K}$ [Figs. 4(a), 4(c), and 4(e)] with the data along $\overline{M}$-$\overline{\Gamma}$-$\overline{M}$ [Figs. 4(b), 4(d), and 4(f)]. The former shows a clear zero CD at k_y=0.

Our circular dichroism measurements provide information about the distinct character of the Dirac dispersions observed in $PtTe_2$ and $PdTe_2$. Figures 4(a), 4(b), 4(e), and 4(f) show the dichroic signal measured at binding energies close to the Fermi level. The type-II cones, expected at ≈ -1 and ≈ -0.6 eV for $PtTe_2$ and $PdTe_2$ respectively (top brown arrows), show a similar dichroism for both compounds, with no switching of the dichroic signal across the Dirac point. In contrast, the surface states in these compounds previously predicted to have a nontrivial topological character [-2.25 eV for $PtTe_2$ and -1.7 eV for $PdTe_2$, bottom black arrows in Figs. 4(c)–4(f)] present a clear switching of the dichroic signal across the Dirac point. This is reminiscent of the circular dichroism measurements performed during the early times of topological insulators, that were identified as mimicking the warped spin texture of the surface states in those materials [36]. The observation of a different circular dichroism for these Dirac dispersions, the type-II Dirac cone and the Dirac surface states, confirms their dissimilar nature. Although both are consequences of a band inversion, time-reversal symmetry, and spin-orbit coupling, their properties differ fundamentally. As mentioned in the Introduction, one is at the bulk, it is formed by a four-band crossing (the Dirac point is fourfold degenerate), and, most importantly, it is only protected by crystalline symmetries. The second one is at the surface, it is nondegenerate, it has a chiral character (it is spin polarized), and it is topologically protected. In the past, some differences in the circular dichroic signal were reported for the bulk and surface state of $PdTe_2$ at ≈ -0.6 and ≈ -1.7 eV respectively [18]. Here, we show a clear switching of the dichroic signal across the M-Γ-A plane ($k_y = 0$) for the type-II cone (both in electron and hole bands), not only for $PdTe_2$ but also for $PtTe_2$ [Figs. 4(a), 4(b), 4(e), and 4(f), top brown arrows). Additionally, we see a clear difference when compared to the surface state cone in both compounds, that switches dichroic signal not only at k_y=0, but also at the binding energy corresponding to the Dirac point [Figs. 4(c)–4(f), bottom black arrows]. The fact that we observe this difference in the circular dichroism for the two Dirac dispersions in the same scan [Figs. 4(c)–4(f)] rules out geometric or final state effects.

We see in our CD data signatures of an additional dispersion already visible using linearly polarized light (Fig. 1 blue arrows), indicated also with blue arrows in Figs. 4(c)–4(f). The data in Fig. 4 were taken at a photon energy very close to the bottom type-II Dirac cone and therefore to A, where our DFT calculations predict this dispersion to appear (see Fig. 2, blue dots). Interestingly, this dispersion shows no switching in the dichroic signal across the higher energy and lower energy states for $PtTe_2$ and a clear switching for $PdTe_2$. Data for another sample of $PdTe_2$, presented in Fig. S4 of Supplemental Material [21], show the same behavior. In the following, we study the dipole matrix element $M_{\mathbf{k}} = \sum_{f,in} |\langle f|\boldsymbol{A}(\omega)\cdot\boldsymbol{j}|in\rangle|^2$ to understand our observation, where $\boldsymbol{A}(\omega)$ is the gauge field of the incident light, $\boldsymbol{j}$ is the electron current, and the sum is over the spin-degenerate final and initial states. We consider $\boldsymbol{A}(\omega) = A_0(\omega)(\sin(\theta_0), i, -\cos(\theta_0))$ with $\theta_0 = 25^\circ$, the incident light angle with respect to the surface of the sample [see Fig. 4(a)]. The initial state $|\text{in}\rangle$ is a Bloch state generally expressed as $|\text{in}\rangle = \sum_l u_{l\mathbf{k}}|l_{\text{in}}\rangle$ with $|l_{\text{in}}\rangle$, and $l = 1, 2, 3, 4$ corresponds to the four eigenstates of the C_3 operator. For the final states, we consider spin-degenerate states in the bulk, denoting them as $|\uparrow_f\rangle$ and $|\downarrow_f\rangle$. By considering the constraints imposed by time-reversal symmetry, inversion symmetry, threefold rotation symmetry, and the mirror-y symmetry, we identify that only $\langle\uparrow_f|j_z|1/3_i\rangle$, $\langle\downarrow_f|j_z|2/4_i\rangle$, $\langle\uparrow_f|j_x - ij_y|2/4_i\rangle$, and $\langle\downarrow_f|j_x + ij_y|1/3_i\rangle$ are nonzero, which allows us to write down a close formula for $M_{\mathbf{k}}$. We then calculate the difference of $M_{\mathbf{k}}$ for the right and left circularly polarized light, $\Delta M_{\mathbf{k}}$, and reveal its dependence on $u_{l\mathbf{k}}$. Details of the symmetry analysis and calculation of $\Delta M_{\mathbf{k}}$ can be found in Supplemental Material, Sec. H [21].

To understand the different dichroism observed in $PtTe_2$ and $PdTe_2$, we consider a symmetry allowed $\mathbf{k}\cdot\mathbf{p}$ Hamiltonian around the A point for the four related bands:

$$H(k_x, k_y, k_z) = t_1(k_x\tau_x\sigma_x + k_y\tau_x\sigma_y) + \left(M + \lambda k_z^2\right)\tau_z\sigma_0 + t_2 i(k_+^3 - k_-^3)\tau_x\sigma_z, \quad (1)$$

where t_1 is a parameter of the form $\hbar v$ with v the group velocity of the modes near the high symmetry point A, and t_2 has units of energy/length^3. M is a parameter that quantifies the energy separation of the four bands at A, λ is of the form $\hbar^2/2m_{\text{eff}}$ with m_{eff} the effective mass of the electrons near the high symmetry point A, and $k_\pm = k_x \pm ik_y$. The introduction of terms linear in k_x and k_y is natural and finds support from our ARPES data and DFT calculations. The term cubic in k_x and k_y is symmetry allowed and relevant to the dichroism. If the linear term dominates ($t_1 \gg t_2$), the eigenstates lead to a $\Delta M_{f\mathbf{k}}$ that has the same sign for the higher and lower energy bands, but changes sign for opposite momentum, consistent with our observation for $PtTe_2$. On the other hand, if the cubic term in k dominates, $\Delta M_{f\mathbf{k}}$ will change sign upon both energy flip and momentum flip, which is consistent with the observation for $PdTe_2$. We propose that despite $PtTe_2$ and $PdTe_2$ belonging to the same space group, a cubic term can be significant in one material but negligible in the other. This difference leads to discernible dichroism behaviors between the two materials. This understanding is also consistent with our DFT calculations in Fig. 2, where the dispersion of $PtTe_2$ (encircled by blue dots) appears to be more linear.

The symmetry operations allowed by the crystallographic space group $P\bar{3}m1$ are at the origin of the most important electronic dispersions in $PtTe_2$ and $PdTe_2$, namely, the bulk

type-II Dirac cones and the topologically protected surface states. Indeed, it has been demonstrated that a perturbation that breaks the trigonal symmetry of the system not only removes the type-II Dirac cones, but also significantly affects the surface states, which are observable in ARPES experiments [5]. Here we have shown that even symmetry preserved perturbations can lead to experimentally discernible ARPES features by using circularly polarized light.

Finally, it is worth noting that overall, some of the symmetries of the crystals $PtTe_2$ and $PdTe_2$ can be easily identified in the measured and calculated band structure for these materials. For example, it can be noted that the dispersion along the $\overline{K}$-$\overline{\Gamma}$-$\overline{K}$ direction is always symmetric with respect to Γ in both compounds [Figs. 3(c) and 3(f)], in contrast to the dispersion along the $\overline{M}$-$\overline{\Gamma}$-$\overline{M}$ direction [Figs. 3(d) and 3(g)]. This threefold symmetry is a consequence of the centrosymmetric trigonal crystal structure of the $PtTe_2$ and $PdTe_2$ crystals, with mirror planes along M-Γ-A as previously described. Additionally, the inversion symmetry present in these crystals relates the energy of the bands at opposite momenta, $E_\sigma(k_x, k_y, k_z) = E_\sigma(-k_x, -k_y, -k_z)$. This can be seen in our data and DFT calculations represented in Fig. S6 of Supplemental Material [21], where a clear signature of such inversion symmetry is observed for $PtTe_2$.

IV. CONCLUSIONS

In conclusion, we have performed a detailed study of the electronic structure of the type-II Dirac semimetals $PtTe_2$ and $PdTe_2$ using high resolution ARPES and DFT calculations, finding a three-dimensional dispersion in these compounds, at -1.4 eV for $PtTe_2$ and -1.1 eV for $PdTe_2$, which presents a distinct signature in $PtTe_2$ and $PdTe_2$ when using circularly polarized light. While $PdTe_2$ shows a clear switching of the dichroic signal across the higher energy and lower energy states, the switching is absent for $PtTe_2$. We relate this observation to the symmetry of the dipole matrix element. After considering the most general Hamiltonian that complies with all the symmetries of both $PtTe_2$ and $PdTe_2$, the contrasting CD signal for both compounds can be explained if one considers that a linear term in momentum dominates in the case of $PtTe_2$ and a cubic term in the case of $PdTe_2$. It is interesting to realize that while the two cases may be hard to distinguish by just looking at the dispersion, there is a clear difference when analyzing the CD.

Our CD measurements put also in evidence the prominent difference between the previously reported Dirac dispersions in these materials. The type-II Dirac cone that lives in the bulk, formed by four bands, protected by the symmetries of the crystal and hosting exotic type-II Dirac fermions, shows no switching of the dichroic signal across the Dirac point. In contrast, the surface state Dirac cone that is formed at the band gap between two bands, topologically protected and hosting chiral Dirac fermions, shows a clear switching of the dichroic signal across the Dirac point.

Our paper not only provides a useful reference for the characterization of other transition metal dichalcogenides with topological properties, but more generally, it shows how circular dichroism in ARPES can be useful in distinguishing the topological character of two seemingly equivalent band dispersions, and may give information about the order of the momentum terms that make up such dispersion.

ACKNOWLEDGMENTS

The primary funding for this work was provided by the U.S. Department of Energy, Office of Science, Office of Basic Energy Sciences under Contract No. DE-SC0018154. I.P., D.B., M.N., and T.H. were supported by the California State University Long Beach (CSULB) and Ohio State University Partnership for Education and Research in Hard and Soft Materials, a NSF PREM, under Grant No. 2122199 for traveling to the ALS. J.E.G., A.J.W., and W.L.B.H. acknowledge the Center for Emergent Materials, an NSF MRSEC, under Grant No. DMR-2011876 for crystal growth and P.Z., and Y.-M.L. for the theoretical symmetry analysis. J.Q. and W.W. acknowledge the AFOSR for funding from Grant No. FA9550-21-1-02684 for theoretical calculations. Calculations were performed at the Ohio Supercomputer Center under Project No. PAS0072. The Advanced Light Source is supported by the Director, Office of Science, Office of Basic Energy Sciences, of the U.S. Department of Energy under Contract No. DE-AC02-05CH11231. The photoemission work by L.M. and A.L. was supported by U.S. Department of Energy, Office of Science, Office of Basic Energy Sciences, Materials Sciences and Engineering Division under Contract No. DE-AC02-05CH11231 within the vdW heterostructure Program (KCWF16). We would like to acknowledge very useful discussions with Mark O. Goerbig, Jean-Noël Fuchs, Frédéric Piéchon, and Alberto Crepaldi. I.P., D.B., and M.N. would like to acknowledge the CSULB Google American Physical Society Bridge Program Fellowship and internal CSULB fellowships such as the John E. Fredrickson Scholarship, the graduate RSCA award, the graduate student honors award, and the Richard D. Green Graduate Research Fellowship from the College of Natural Sciences and Mathematics at CSULB.

[1] B.-J. Yang and N. Nagaosa, Classification of stable three-dimensional Dirac semimetals with nontrivial topology, Nat. Commun. **5**, 4898 (2014).

[2] B. Q. Lv, T. Qian, and H. Ding, Experimental perspective on three-dimensional topological semimetals, Rev. Mod. Phys. **93**, 025002 (2021).

[3] Y. Xu, F. Zhang, and C. Zhang, Structured Weyl points in spin-orbit coupled fermionic superfluids, Phys. Rev. Lett. **115**, 265304 (2015).

[4] A. A. Soluyanov, D. Gresch, Z. Wang, Q. Wu, M. Troyer, X. Dai, and B. A. Bernevig, Type-II Weyl semimetals, Nature (London) **527**, 495 (2015).

[5] H. Huang, S. Zhou, and W. Duan, Type-II Dirac fermions in the $PtSe_2$ class of transition metal dichalcogenides, Phys. Rev. B **94**, 121117(R) (2016).

[6] H. Gao, J. W. F. Venderbos, Y. Kim, and A. M. Rappe, Topological semimetals from first principles, Annu. Rev. Mater. Res., **49**, 153 (2019)

[7] S. M. Young, S. Zaheer, J. C. Y. Teo, C. L. Kane, E. J. Mele, and A. M. Rappe, Dirac semimetal in three dimensions, Phys. Rev. Lett. **108**, 140405 (2012).

[8] S. M. Young and C. L. Kane, Dirac semimetals in two dimensions, Phys. Rev. Lett. **115**, 126803 (2015).

[9] C. Niu, H. Wang, N. Mao, B. Huang, Y. Mokrousov, and Y. Dai, Antiferromagnetic topological insulator with nonsymmorphic protection in two dimensions, Phys. Rev. Lett. **124**, 066401 (2020).

[10] B.-J. Yang, T. Morimoto, and A. Furusaki, Topological charges of three-dimensional Dirac semimetals with rotation symmetry, Phys. Rev. B **92**, 165120 (2015).

[11] Z. Wang, Y. Sun, X.-Q. Chen, C. Franchini, G. Xu, H. Weng, X. Dai, and Z. Fang, Dirac semimetal and topological phase transitions in A_3 Bi (A = Na, K, Rb), Phys. Rev. B **85**, 195320 (2012).

[12] Z. Wang, H. Weng, Q. Wu, X. Dai, and Z. Fang, Three-dimensional Dirac semimetal and quantum transport in Cd_3As_2, Phys. Rev. B **88**, 125427 (2013).

[13] Z. K. Liu, B. Zhou, Y. Zhang, Z. J. Wang, H. M. Weng, D. Prabhakaran, S.-K. Mo, Z. X. Shen, Z. Fang, X. Dai, Z. Hussain, and Y. L. Chen, Discovery of a three-dimensional topological Dirac semimetal, Na_3Bi, Science **343**, 864 (2014).

[14] M. Neupane, S.-Y. Xu, R. Sankar, N. Alidoust, G. Bian, C. Liu, I. Belopolski, T.-R. Chang, H.-T. Jeng, H. Lin, A. Bansil, F. Chou, and M. Z. Hasan, Observation of a three-dimensional topological Dirac semimetal phase in high-mobility Cd_3As_2, Nat. Commun. **5**, 3786 (2014).

[15] S. Borisenko, Q. Gibson, D. Evtushinsky, V. Zabolotnyy, B. Buchner, and R. J. Cava, Experimental realization of a three-dimensional Dirac semimetal, Phys. Rev. Lett. **113**, 027603 (2014).

[16] Z. K. Liu, J. Jiang, B. Zhou, Z. J. Wang, Y. Zhang, H. M. Weng, D. Prabhakaran, S.-K. Mo, H. Peng, P. Dudin, T. Kim, M. Hoesch, Z. Fang, X. Dai, Z. X. Shen, D. L. Feng, Z. Hussain, and Y. L. Chen, A stable three-dimensional topological Dirac semimetal Cd_3As_2, Nat. Mater. **13**, 677 (2014).

[17] M. Yan, H. Huang, K. Zhang, E. Wang, W. Yao, K. Deng, G. Wan, H. Zhang, M. Arita, H. Yang, Z. Sun, H. Yao, Y. Wu, S. Fan, W. Duan, and S. Zhou, Lorentz-violating type-ii dirac fermions in transition metal dichalcogenide $PtTe_2$, Nat. Commun. **8**, 257 (2017).

[18] H.-J. Noh, J. Jeong, E.-J. Cho, K. Kim, B. I. Min, and B.-G. Park, Experimental realization of type-II Dirac fermions in a $PdTe_2$ superconductor, Phys. Rev. Lett. **119**, 016401 (2017).

[19] Y. Liu, J.-Z. Zhao, L. Yu, C.-T. Lin, A.-J. Liang, C. Hu, Y. Ding, Y. Xu, S.-L. He, L. Zhao, G.-D. Liu, X.-L. Dong, J. Zhang, C.-T. Chen, Z.-Y. Xu, H.-M. Weng, X. Dai, Z. Fang, and X.-J. Zhou, Identification of topological surface state in $PdTe_2$ superconductor by angle-resolved photoemission spectroscopy*, Chin. Phys. Lett. **32**, 067303 (2015).

[20] R. Moessner and J. E. Moore, Frontmatter, *Topological Phases of Matter* (Cambridge University, New York, 2021), p. 228.

[21] See Supplemental Material at http://link.aps.org/supplemental/10.1103/PhysRevB.110.195429 for details of the crystal growth, the unit cell of the $PtTe_2$ and $PdTe_2$ space group, additional photoemission and circular dichroism data for $PdTe_2$, second derivative of the type-II cones of $PtTe_2$ and $PdTe_2$, tables listing the correspondence between k_z and photon energy for both compounds, details on our symmetry analysis of the circular dichroism, additional data for $PtTe_2$ that show signature of the inversion symmetry in this crystal, and which also contains Refs. [22,23].

[22] Edited by M. I. Aroyo, *International Tables for Crystallography* (International Union of Crystallography, Chester, England, 2016).

[23] Topological material database, http://topologicalquantumchemistry.org/.

[24] W. L. B. Huey, A. M. Ochs, A. J. Williams, Y. Zhang, S. Kraguljac, Z. Deng, C. E. Moore, W. Windl, C. N. Lau, and J. E. Goldberger, $Cr_xPt_{1-x}Te_2 (x \leqslant 0.45)$: A family of air-stable and exfoliatable van der Waals ferromagnets, ACS Nano **16**, 3852 (2022).

[25] G. Kresse and J. Hafner, *Ab initio* molecular dynamics for liquid metals, Phys. Rev. B **47**, 558 (1993).

[26] G. Kresse and J. Hafner, *Ab initio* molecular-dynamics simulation of the liquid-metal–amorphous-semiconductor transition in germanium, Phys. Rev. B **49**, 14251 (1994).

[27] P. E. Blöchl, Projector augmented-wave method, Phys. Rev. B **50**, 17953 (1994).

[28] J. P. Perdew, K. Burke, and M. Ernzerhof, Generalized gradient approximation made simple, Phys. Rev. Lett. **77**, 3865 (1996).

[29] G. Kliche, Far-infrared and x-ray investigations of the mixed platinum dichalcogenides PtS_{2-x} Se_x, $PtSe_{2-x}$ Te_x, and PtS_{2-x} Te_x, J. Solid State Chem. **56**, 26 (1985).

[30] E. L. Hoffman and W. H. MacLean, Phase relations of michenerite and merenskyite in the Pd-Bi-Te system, Economic Geology **71**, 1461 (1976).

[31] O. J. Clark, M. J. Neat, K. Okawa, L. Bawden, I. Marković, F. Mazzola, J. Feng, V. Sunko, J. M. Riley, W. Meevasana, J. Fujii, I. Vobornik, T. K. Kim, M. Hoesch, T. Sasagawa, P. Wahl, M. S. Bahramy, and P. D. C. King, Fermiology and superconductivity of topological surface states in $PdTe_2$, Phys. Rev. Lett. **120**, 156401 (2018).

[32] M. S. Bahramy *et al.*, Ubiquitous formation of bulk Dirac cones and topological surface states from a single orbital manifold in transition-metal dichalcogenides, Nat. Mater. **17**, 21 (2018).

[33] M. R. Scholz, J. Sánchez-Barriga, J. Braun, D. Marchenko, A. Varykhalov, M. Lindroos, Y. J. Wang, H. Lin, A. Bansil, J. Minár, H. Ebert, A. Volykhov, L. V. Yashina, and O. Rader, Reversal of the circular dichroism in angle-resolved photoemission from Bi_2 Te_3, Phys. Rev. Lett. **110**, 216801 (2013).

[34] C. Bigi, F. Mazzola, J. Fujii, I. Vobornik, G. Panaccione, and G. Rossi, Measuring spin-polarized electronic states of quantum materials: 2H-$NbSe_2$, Phys. Rev. B **103**, 245142 (2021).

[35] F. Vidal, M. Eddrief, B. Rache Salles, I. Vobornik, E. Velez-Fort, G. Panaccione, and M. Marangolo, Photon energy dependence of circular dichroism in angle-resolved

photoemission spectroscopy of Bi_2Se_3 Dirac states, Phys. Rev. B **88**, 241410(R) (2013).

[36] Y. H. Wang, D. Hsieh, D. Pilon, L. Fu, D. R. Gardner, Y. S. Lee, and N. Gedik, Observation of a warped helical spin texture in Bi_2 Se_3 from circular dichroism angle-resolved photoemission spectroscopy, Phys. Rev. Lett. **107**, 207602 (2011).

[37] Y. Wang and N. Gedik, Circular dichroism in angle-resolved photoemission spectroscopy of topological insulators, Phys. Rap. Res. Ltrs. **7**, 64 (2013).

[38] C. M. Schneider and J. Kirschner, Spin- and angle-resolved photoelectron spectroscopy from solid surfaces with circularly polarized light, Crit. Rev. Solid State Mater. Sci. **20**, 179 (1995).